A piezoelectric nonlinear energy sink shunt for vibration damping

Kevin Dekemele[1,*], Christophe Giraud-Audine[b], Olivier Thomas[c]

[a] *Ghent University, Department of Electromechanical, Systems and Metal Engineering, Tech Lane Ghent Science Park - Campus A 125, 9052, Ghent, Belgium*
[b] *Arts et Métiers Institute of Technology, L2EP, Univ. Lille, Centrale Lille, JUNIA, F-59000 Lille, France*
[c] *Arts et Métiers Institute of Technology, LISPEN, F-59000 Lille, France*

Abstract

The theoretical study and experimental validation of a nonlinear shunt circuit for piezoelectric vibration damping is investigated here. The circuit consists of a resistor, an inductor and a nonlinear cubic voltage source. The shunt acts as an electrical analog to the mechanical nonlinear energy sinks (NESs). These mechanical NESs are passive vibration absorbers that typically have a cubic nonlinear stiffness. They have attractive properties such as saturation of the host system's vibration amplitude and strongly modulated response. This increases its operational frequency bandwidth and robustness against variations in the properties of host systems compared to linear vibration absorbers. However, the nonlinear nature may induce isolated responses in the host system that induce high vibration amplitudes. This paper investigates if these attractive properties also occur in the electric nonlinear energy sink shunt. An analytical expression for the frequency response is derived through the complexification-averaging method. Bifurcations in the frequency response reveal the occurrence of a quasi-periodic vibration energy exchange between the host system and the voltage over the electrodes of piezoelectric material. This is the main mechanism behind the amplitude saturation of the host system. Other bifurcations also reveal the existence of isolated responses. The nonlinear shunt is then realized with analog multipliers and a synthetic inductor and its performance in vibration damping is experimentally verified for a cantilever beam.

Keywords: Piezoelectric Vibration Damping, Nonlinear Energy Sink, Nonlinear Shunt

---

[*] Corresponding Author
Email address: `kevin.dekemele@ugent.be` (Kevin Dekemele)

1. Introduction

Mechanical vibrations affect structural integrity, machine performance and health of operators/inhabitants. A widely used way to mitigate the vibrations is to add an additional mechanical degree of freedom to the host system, called a vibration absorber. This absorber is designed such that its oscillations create forces that counteract the external excitation and dissipate energy in a completely passive way. The most common vibration absorber is the tuned-mass-damper (TMD), which is an oscillator consisting of an inertia, a linear spring, and a linear damper [1, 2, 3] or a Lanchester damper, only composed of an inertia and a viscous damper [4]. Many designs exist, including using pendulums [5, 6] or rotating inertias [7]. In each case, TMDs require tuning on a targeted vibration mode of the host system and show a limited bandwidth as they only operate efficiently around the tuned frequency. They thus perform poorly if the frequency of vibration changes or if the vibration consists of multiple frequencies.

To tackle these limitations, the nonlinear energy sink concept (NES) has been proposed in the pioneering work [8, 9] and later experimentally verified, [10, 11], a vibration absorber that has some nonlinearities, commonly a nonlinear spring. Because of these nonlinearities, the natural frequency is variable as a function of the vibration amplitude, enabling the NES to self-tune to the host system frequency for a certain range of amplitude. This leads to a one-way energy transfer, called targeted energy transfer, toward the NES which, in turn, dissipates it.. Furthermore, unlike the TMD, the NES can dissipate several frequencies efficiently in a sequential manner through resonance capture cascade [12, 13, 14, 15] and can also stabilize instabilities such as chatter, aeroelastic and friction-induced instabilities [16, 17, 18, 19]. The NES can also serve as an efficient vibration absorber if the host system also includes nonlinearities [20, 21, 22]. Although the nonlinear stiffness is usually a hardening cubic polynomial, other characteristics include bistable [23, 24], non-smooth piecewise linear/nonlinear stiffness [25, 26], softening nonlinear stiffness [15, 27, 28] and hardening-softening nonlinear stiffness [29, 30]. Some works also incorporate nonlinear damping [31, 32, 28]. Configurations featuring more complex NESs consisting of several degrees-of-freedom have also been investigated, [33, 34, 35]. Finally, the NES can be employed a broadband isolator or enhance existing ring isolators [36, 37]

A harmonically forced host system with a mechanical NES [38, 39] has three characteristic properties. The first one is that, given sufficient energy, the vibration amplitude in the host structure will saturate even as the forcing level increases. This contrasts sharply with linear absorbers, where the amplitude scales with the force. The second property is the strongly modulated response (SMR). In this quasi-periodic response, the vibrations have a slow modulation, and energy is continuously exchanged between the host system and the NES. The SMR is triggered at the saturation amplitude of the host system. The third property is the existence of isolated responses. These are isolated curves on the frequency response that have a high amplitude in the host system and, as such, are undesirable responses. The isolated curves are reached under certain initial conditions. This isolated curve can even attach to the main response curve for high forcing levels, which is detrimental to the NES's performance. The first two properties are attractive for vibration control, while the third should be avoided as it limits the operational range of the NES. As such, tuning a mechanical NES exists in defining a forcing range where the host system's response saturates, without attachment of isolated response to the main branch of the frequency response [32].

All the vibration absorbers mentioned so far are mechanical devices, that add weight to the host system and need a clearance space to vibrate, which might not be acceptable for innovative mechanical designs that strive for compactness and light-weightness to reduce energy costs. A possible strategy to overcome these issues is to rely on piezoelectric shunts, which are electromechanical analogs of the mechanical absorbers, an idea proposed in the pioneering work [40]. They consist of bonding piezoelectric transducers to the host mechanical structure, in order to couple the mechanical system to an electric circuit (called the shunt), which plays the role of the vibration absorber. An analog to the TMD is obtained with a linear electrical oscillator by connecting the piezoelectric transducer, which acts as a capacitor, to a shunt circuit composed of an inductor and a resistor. As this so-called resonant shunt works similarly as a TMD [41, 7] it thus shares its limitations in terms of small operational bandwidth [41, 42, 43]. The performance of this linear passive circuit can be somewhat enhanced by adding more complex circuitry, such as negative capacitance [44], several parallel shunted piezoelectric transducers [45] or electrical analogs of the discretized host structure for broadband damping [46], among other techniques (see the recent reviews [47, 48]).

Then, similary as for mechanical designs, adding nonlinearities in the electric circuits seems an attractive idea since designing nonlinear electronic circuits may appear simpler than mechanical nonlinearities. A first concept is based on mirroring the nonlinearities of the host system in the absorber. This strategy was introduced in a piezoelectric shunt in [49] and experimentally demonstrated in [50, 51] with passive electronic components and in [52] with a digital signal processor. A second strategy is the so-called synchronized switch damping techniques, proposed in [53] and is addressed in many theoretical and experimental studies since [54, 48]. A third strategy is based on the use of internal resonances, which leads to strong energy transfers between vibration modes when their natural frequencies are tuned in an integer ratio. The case of a mechanical mode tuned at twice the frequency of an electrical oscillator (a so-called 1:2 internal resonance) was explored in the series of papers [55, 56, 57, 58], leading to an interesting saturation phenomenon, for which the vibration amplitude of the host structure is independent of an increase of the input forcing. A 1:3 internal resonance was also investigated in [59]. Recently, synthesizing a Duffing oscillator in the electronic circuit was demonstrated with a digital controller [60]. It was also demonstrated that a non-smooth nonlinearity, realized by a diode in the shunt circuit, enables the tuning of a resonant shunt [61].

Given the attractive properties of the mechanical NES discussed above, it will be investigated here if a piezoelectric NES shunt can be made that has the aforementioned behavior. The saturation effect for mechanical NES, acting in 1:1 resonance, is typically very robust to parameter changes and acts over a wide frequency band. This study's goal and novelty here is to theoretically and experimentally show the proof-of-concept of a piezoelectrical NES shunt using a cubic voltage source as nonlinearity. Up to now, only a few papers mention investigating piezoelectric NESs, and use a cubic capacitor concept, while this paper will use the cubic voltage source. It was theoretically investigated in [62, 59] and experimentally realized in [63, 64] with analog multipliers to create a nonlinear cubic capacitor component and [65] in an active control philosophy with force feedback. In [66], a multiplier circuit was proposed to shunt a loudspeaker NES, but was not implemented. In comparison to the previous works, here a full design methodology of a piezoelectric NES with a cubic voltage source will be shown, based on models and analog electronic circuit designs strategy already introduced in [56, 57]. These two works, however, used the polynomial voltage source to achieve a different vibration energy mechanism, the 1:2 internal resonance. The design that will be proposed here does not rely on canceling the capacitance of the piezoelectric patch with a negative capacitance as in [63], and is thus less sensitive to possible instabilities. Also, as pointed out in [55], the polynomial voltage circuit required less electronic gain than a cubic capacitor circuit, implying an easier and more widely applicable circuit implementation. Finally, unlike other works before, this paper will fully explore the above-mentioned features of saturation, strongly modulated response, and isolates in the context of piezoelectric shunts.

The work is structured as follows: in section two, the equations of motion of the coupled mechanical-piezoelectrical system are presented and made dimensionless. The frequency response is derived in section three using the Complexification-averaging technique. Some numerical simulations will show the three typical NES characteristic vibration regimes and the conditions for the isola are studied. The experimental setup, circuit and results are presented in section four. Finally, the conclusions are presented.

2. Theoretical description and tuning

2.1. Equations of motion

We consider a linear elastic mechanical structure on which a piezoelectric patch is bonded. The patch's electrodes are connected to an inductor and resistor, which

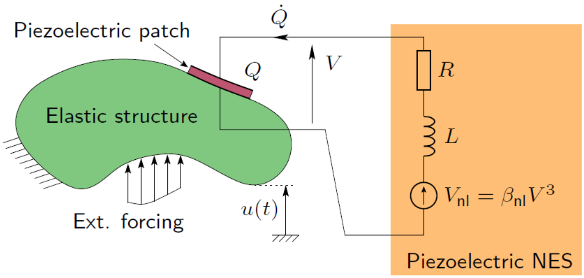

Figure 1: An elastic elastic structure coupled to a nonlinear electric circuit through a piezoelectric patch.

forms a resonant electronic circuit together with the patch's self-capacitance. The circuit also includes a nonlinear voltage source V_{nl} as shown in Figure 1.

Considering a modal model of the linear structure excited by a harmonic external forcing, the governing equations of the problem are [67]:

$$\mathbf{M}\ddot{\mathbf{q}} + \mathbf{C}\dot{\mathbf{q}} + \boldsymbol{\Omega}\mathbf{q} + \boldsymbol{\Theta}V = \mathbf{F}\cos(\omega t), \tag{1a}$$

$$C_{\text{p}}V - Q - \boldsymbol{\Theta}^T\mathbf{q} = 0, \tag{1b}$$

$$V + L\ddot{Q} + R\dot{Q} + V_{\text{nl}} = 0, \tag{1c}$$

where $\mathbf{q}(t) \in \mathbb{R}^{N\times 1}$ gathers the mechanical modal coordinates at time t, $V(t)$ is the voltage at the terminals of the piezoelectric patch and $Q(t)$ is the electric charge contained in its electrodes. Those governing equations are obtained by expanding the displacement field of the structure onto $N \in \mathbb{N}$ *short-circuit* eigenmodes, *i.e.* computed with $V = 0$. Then, $\boldsymbol{\Omega} = \text{diag}(\breve{\omega}_1, \dots \breve{\omega}_N)$ is the diagonal matrix that gathers the short-circuit natural frequencies $\breve{\omega}_i$, $\mathbf{M} = \text{diag}(m_1, \dots m_N)$ gathers the modal masses m_i, $\mathbf{C} \in \mathbb{R}^{N\times N}$ is the damping matrix and $\mathbf{F} \in \mathbb{R}^{N\times 1}$ is the external force vector. On the piezoelectric side, $\boldsymbol{\Theta} = [\theta_1, \dots \theta_N]^{\text{T}} \in \mathbb{R}^{N\times 1}$ is the modal electromechanical coupling vector, C_{p} is the electrical capacitance of the piezoelectric patch and (L, R) are the inductance and the resistance.

The nonlinear voltage source in the shunt depends on the voltage at the terminals $V(t)$ and is chosen here as a hardening (i.e. with coefficient $\beta_{\text{nl}} > 0$) cubic nonlinearity:

$$V_{\text{nl}} = \beta_{\text{nl}} V^3. \tag{2}$$

From an electronic circuitry point of view, the electrode's voltage V is easily monitored, and cubing the voltage is practically done with multipliers. In [55], it was shown that a nonlinear voltage has a similar effect as a purely nonlinear capacitor, with the added benefit that it is much easier to realize. Considering the dynamical behavior of the system reduced to its ith linear mode ($q_k = 0\ \forall k \neq i$), Eq. (1b) reduces to:

$$C_\mathrm{p}V - Q - \theta_i q_i = 0. \tag{3}$$

The cube of this voltage results in a cubed capacitance and displacement term, plus mixed terms. Then, eliminating V with Q in Eqs. (1a,c), by using Eq. 3 the following equations of motion (EOM) are obtained:

$$\ddot{q}_i + 2\zeta_i\omega_i\dot{q}_i + \omega_i^2 q_i + \frac{\theta_i}{m_i C_\mathrm{p}}Q = \frac{F_i}{m_i}\cos(\omega t), \tag{4a}$$

$$\ddot{Q} + 2\zeta_e\omega_e\dot{Q} + \omega_e^2 Q + \frac{\theta_i}{LC_\mathrm{p}}q_i + \frac{V_\mathrm{nl}}{L} = 0, \tag{4b}$$

where m_i is the modal mass of mode i, ζ_i is the modal damping of mode i, θ_i is the modal electromechanical coupling of mode i, ω_e is the electrical eigenfrequency and ζ_e is the electrical damping factor. The last two are defined as:

$$\omega_e = \sqrt{\frac{1}{LC_\mathrm{p}}}, \quad \zeta_e = \frac{R}{2}\sqrt{\frac{C_\mathrm{p}}{L}}. \tag{5}$$

Moreover, ω_i, such that $\omega_i^2 = \breve{\omega}_i^2 + \theta_i^2/(C_\mathrm{p}m_i)$, is an approximation (because of the one mode expansion, see [67, 41]) of the ith *open-circuit* natural frequency (*i.e.* computed with $Q = 0$ in Eq. (1)). It enables defining the (dimensionless) ith electromechanical modal coupling factor as [68]:

$$k_i^2 = \frac{\omega_i^2 - \breve{\omega}_i^2}{\omega_i^2} = \frac{\theta_i^2}{\omega_i^2 C_{\mathrm{p}i} m_i}. \tag{6}$$

It is then convenient to scale the governing equations (4) to reduce the number of independent parameters. The following dimensionless time τ, dimensionless modal displacement $\bar{q}_i$, dimensionless electric charge $\bar{Q}$ and dimensionless piezoelectric voltage $\bar{V}$, are defined as:

$$\tau = \omega_i t, \quad \bar{q}_i = \sqrt{m_i\gamma}q_i, \quad \bar{Q} = \sqrt{\gamma L}Q, \quad \bar{V} = \frac{\sqrt{\gamma}}{\omega_i^2\sqrt{L}}V, \quad \gamma = \frac{\beta_\mathrm{nl}\omega_i^2}{C_\mathrm{p}} \tag{7}$$

such that the governing Eqs (3) and (4) in dimensionless form using Eqs (7) become:

$$\bar{q}_i'' + 2\zeta_i\bar{q}_i' + \bar{q}_i + k_i r_i\bar{Q} = \bar{F}_i\cos(\Omega\tau), \tag{8a}$$

$$\bar{Q}'' + 2\zeta_e r_i\bar{Q}' + r_i^2\bar{Q} + k_i r_i\bar{q}_i + \bar{V}_\mathrm{nl} = 0, \tag{8b}$$

$$\bar{V} = r_i^2\bar{Q} + k_i r_i\bar{q}_i, \tag{8c}$$

where

$$r_i = \frac{\omega_e}{\omega_i}, \quad \circ' = \frac{d\circ}{d\tau}, \quad \Omega = \frac{\omega}{\omega_i}, \quad \bar{F}_i = \frac{\sqrt{\gamma}F_i}{\omega_i^2\sqrt{m_i}}. \tag{9}$$

with $'$ meaning the derivative in dimensionless time. The time is rescaled by the open-circuit natural frequency ω_i and the scaling of (q_i, Q) was chosen to have the same coupling factor $k_i r_i$ in Eqs. (8a,b) and also to obtain dimensionless quantities $(\bar{q}_i, \bar{Q})$. Moreover, V was scaled such that the factor of $\bar{V}_{\text{nl}}$ in Eq. (8b) is one. As a consequence, the nonlinear factor β_{nl} (see Eq. (2)), appears through γ in the scaling of all variables (see Eq. (7)).

In the next step, only the voltage is kept as the electric coordinate, where $\bar{Q}$ is eliminated using Eq. (8c) to obtain:

$$\bar{q}_i'' + 2\zeta_i \bar{q}_i' + (1 - k_i^2)\bar{q}_i + \frac{k_i}{r_i}\bar{V} = \bar{F}_i \cos(\Omega\tau), \tag{10a}$$

$$\bar{V}'' - r_i k_i \bar{q}'' + 2\zeta_e r_i \left(\bar{V}' - r_i k_i \bar{q}'\right) + r_i^2 \bar{V} + \bar{V}^3 = 0. \tag{10b}$$

Opting for $\bar{V}$ as the electric variable allows to obtain simple polynomial expressions for the frequency response that is derived in the next section.

3. Frequency response

3.1. Complexification averaging method

To obtain the frequency response, the complexification-averaging method (CxA) [69, 9, 70] is applied, which has been extensively used to study the mechanical NESs. This technique involves separating the dynamics into a fast (vibrations) and a slow (amplitude modulation) part by defining complex variables. Subsequently, the amplitude modulations are then averaged over a single period of the proposed vibration frequency. Recently, this technique has been expanded to support averaging over several frequencies, [71, 14]. The first step in the CxA procedure is defining the time-varying complex variables that contain the amplitude modulation, $A \in \mathbb{C}$ and $B \in \mathbb{C}$:

$$2A(\tau)e^{j\Omega\tau} = \bar{q}_i - j\frac{\bar{q}_i'}{\Omega} \qquad 2B(\tau)e^{j\Omega\tau} = \bar{V} - j\frac{\bar{V}'}{\Omega} \tag{11}$$

where $j = \sqrt{-1}$ is the imaginary unit. The original variables $\bar{q}_i$, $\bar{V}$ and their derivatives in functions of A and B are obtained by added and subtracting Eqs. (11) and their complex conjugates:

$$\bar{q}_i = Ae^{j\Omega\tau} + A^* e^{-j\Omega\tau} \qquad \bar{V} = Be^{j\Omega\tau} + B^* e^{-j\Omega\tau} \tag{12a}$$

$$\bar{q}_i' = j\Omega(Ae^{j\Omega\tau} - A^* e^{-j\Omega\tau}) \qquad \bar{V}' = j\Omega(Be^{j\Omega\tau} - B^* e^{-j\Omega\tau}) \tag{12b}$$

where $\circ^*$ is the complex conjugate of $\circ$. The acceleration and second derivative of the voltage as functions of the new variables A and B is found by time derivation of Eqs. (11):

$$2A'e^{j\Omega\tau} + 2j\Omega Ae^{j\Omega\tau} = \bar{q}_i' - j\frac{\bar{q}_i''}{\Omega} \qquad 2B'e^{j\Omega\tau} + 2j\Omega Be^{j\Omega\tau} = \bar{V}' - j\frac{\bar{V}''}{\Omega} \tag{13}$$

Using Eq. (12b), this becomes:

$$\bar{q}_i'' + \Omega^2 \bar{q}_i = j2\Omega A' e^{j\Omega\tau} \qquad \bar{V}'' + \Omega^2 \bar{V} = j2\Omega B' e^{j\Omega\tau} \tag{14}$$

Substituting Eqs. (12) and (14) into Eq. (10), multiplying by $e^{-j\Omega\tau}$ and subsequently averaging with the forcing frequency Ω yields:

$$2jA'\Omega + (1 - k_i^2 - \Omega^2)A + 2j\zeta_i\Omega A + \frac{k_i}{r_i}B = \frac{\bar{F}_i}{2} \tag{15a}$$

$$\begin{aligned} 2jB'\Omega - 2jA'\Omega r_i k_i + (r_i^2 - \Omega^2)B + \Omega^2 A k_i r_i + 2j\Omega\zeta_e r_i(B - k_i r_i A) \\ + 3B^2 B^* = 0 \end{aligned} \tag{15b}$$

These equations are first studied in the steady state, for which $A' = B' = 0$. Rewriting (15b) in the steady state as:

$$\Omega k_i r_i(\Omega - 2j\zeta_e r_i)A = \left((\Omega^2 - r_i^2 + 2j\Omega\zeta_e r_i) - 3BB^*\right) B \tag{16}$$

then using the polar forms $A = \frac{a}{2}e^{j\alpha}$, $B = \frac{b}{2}e^{j\beta}$ and taking the square of the modulus of Eq. (16) leads to obtain a relation between a and b independent of the forcing, called a slow invariant manifold (SIM) in the mechanical NES literature:

$$k_i^2 r_i^2 \Omega^2 \left(\Omega^2 + (2\zeta_e r_i)^2\right) a^2 = \left((2\zeta_e r_i \Omega)^2 + \left(\Omega^2 - r_i^2 - \frac{3}{4}b^2\right)^2\right) b^2. \tag{17}$$

Then, A can be eliminated from Eq. (15a) by using Eq. (16), yielding:

$$\begin{aligned} B\Big(& 3(1 - k_i^2 - \Omega^2)BB^* + (1 - k_i^2 - \Omega^2)\left(r_i^2 - \Omega^2\right) - 4\zeta_i\zeta_e\Omega^2 r_i - k_i^2\Omega^2 \\ & + j\left(3\left(2\zeta_i\Omega\right)BB^* + (1 - \Omega^2)(2\zeta_e r_i\Omega) + 2\zeta_i\Omega\left(r_i^2 - \Omega^2\right)\right)\Big) \\ & = \frac{\bar{F}_i}{2}\left(i2\zeta_e r_i\Omega - \Omega^2\right) k_i r_i. \end{aligned} \tag{18}$$

Taking the square of the modulus of this equation and collecting with power of b yields a relation between the force $\bar{F}_i$ and b:

$$\begin{aligned}
&\left((\frac{3}{4}(1-k_i^2-\Omega^2))^2 + (2\zeta_i\Omega\frac{3}{4})^2 \right) b^6 \\
&+ \Bigg(\frac{3}{2}(1-k_i^2-\Omega^2)((1-k_i^2-\Omega^2)(r_i^2-\Omega^2) - 4\zeta_i\zeta_e\Omega^2 r_i - k_i^2\Omega^2) \\
&+ 3\zeta_i\Omega((1-\Omega^2)(2\Omega\zeta_e r_i) + (2\zeta_i\Omega)(r_i^2-\Omega^2)) \Bigg) b^4 \\
&+ \Bigg(((1-k_i^2-\Omega^2)(r_i^2-\Omega^2) - 4\zeta_i\zeta_e\Omega^2 r_i - k_i^2\Omega^2)^2 \\
&+ ((1-\Omega^2)(2\Omega\zeta_e r_i) + (2\zeta_i\Omega)(r_i^2-\Omega^2))^2 \Bigg) b^2 - \bar{F}_i^2((2\Omega\zeta_e r_i)^2 + \Omega^4)(r_i k_i)^2 = 0
\end{aligned} \tag{19}$$

With Eqs. (19) and (17), the frequency response (FR) can be computed. For a given force $\bar{F}_i$, the roots of the polynomial in b in Eq. (19) are numerically computed for each Ω, obtaining either 1 or 3 solutions in b^2. Then, Eq. (17) is used to obtain a. The complete separation of a and b from their phase counterparts α and β and the analytical expressions as polynomials in Eqs. (17) and (19) was only possible by using $\bar{V}$ as the electric coordinate instead of the charge $\bar{Q}$. Splitting Eqs. (15) for $A' = B' = 0$ into real and imaginary part leads to the following:

$$\bar{F}_i \cos(\alpha) - \frac{k_i}{r_i} b \cos(\beta - \alpha) = (1 - k_i^2 - \Omega^2) a \tag{20a}$$

$$\bar{F}_i \sin(\alpha) + \frac{k_i}{r_i} b \sin(\beta - \alpha) = -2\zeta_i \Omega a \tag{20b}$$

$$\Omega^2 a k_i r_i \cos(\alpha - \beta) + 2\zeta_e r_i^2 k_i \Omega a \sin(\alpha - \beta) = -(r_i^2 - \Omega^2) b - \frac{3}{4} b^3 \tag{20c}$$

$$\Omega^2 a k_i r_i \sin(\alpha - \beta) - 2\zeta_e r_i^2 k_i \Omega a \cos(\alpha - \beta) = -2\zeta_e r_i \Omega b \tag{20d}$$

Having computed a and b, the phases α and β can be determined from Eqs. (20c) and (20d) by eliminating either the sin or cos to obtain $\alpha - \beta$ and then computing α with Eqs. (20a) or (20b).

The final step in the FR computation is determining the stability of the steady-state solutions. Then, the stability is computed numerically from the eigenvalues of the Jacobian of the above Eqs. 15, given in Appendix A. If one of the eigenvalues has a positive real part, the solution is unstable. Furthermore, the change of stability is associated to bifurcations [72], either fold or Neimarck-Sacker in our case.

Numerical examples of frequency responses are depicted in Figure 2a as the thick solid and dashed lines for $\bar{F}_i = [0.15, 0.35, 0.55]$, $r_i = k_i = \zeta_e = 0.2$ and

$\zeta_i = 0.0073$ obtained by computing b with Eq. (19) and then the corresponding a with Eq. (17), alongside the open-circuit linear response in line-dash. The thick lines are stable solutions and the dashed line signifies the unstable ones as found by the Jacobian in Appendix A. Bifurcations for the $\bar{F}_i = 0.55$ curve are indicated by the yellow squares, where B signifies a fold bifurcation and NS a Neimarck-Sacker bifurcation , indicative of the emergence of a quasi-periodic solution. For the same force level, an isola is seen for $\Omega = [0.913,\ 942]$, which limits the effective forcing range of the piezoelectric shunt. The isola is studied in more detail in Section 3.4. The dotted lines a_- and a_+ on the figures are the minima of the SIM in Eq. (17). These points can be computed by deriving Eq. (17) w.r.t. b^2:

$$\frac{\partial a^2}{\partial b^2} = \frac{\frac{27}{16}b^4 - 3b^2\left(\Omega^2 - r_i^2\right) + (2\zeta_e r_i \Omega)^2 + \left(\Omega^2 - r_i^2\right)^2}{k_i^2 r_i^2\left(\Omega^4 + (2\zeta_e r_i \Omega)^2\right)}. \tag{21}$$

The roots of Eq. (21) then reveal the minima and maxima:

$$\begin{aligned} b_\pm^2 &= -\frac{8(r_i^2 - \Omega^2)}{9} \pm \frac{4\sqrt{(r_i^2 - \Omega^2)^2 - 12\zeta_e^2 r_i^2 \Omega^2}}{9}, \\ a_\mp^2 &= \frac{\left((2\zeta_e r_i \Omega)^2 + \left((\Omega^2 - r_i^2) - \frac{3}{4}b_\pm^2\right)^2\right)}{k_i^2 r_i^2\left(\Omega^4 + (2\zeta_e r_i \Omega)^2\right)} b_\pm^2. \end{aligned} \tag{22}$$

Two SIMs, computed with Eq 17, for $\Omega = 1$ and $\Omega = 0.925$ are given in Figure 2b with the maximum and minimum marked for $\Omega = 1$. These points have been shown to be vital in predicting the saturation level of the frequency response and minimum and maximum amplitude during quasi-periodic vibrations of the full EOM for the mechanical NESs [32, 73, 74], but only if there is a small coupling $\epsilon \ll 1$ between the host system and NES equations, typically the NES mass for the mechanical devices. For the piezoelectrical NES, the coupling here is the term $\epsilon = r_i k_i$ in Eq.(8).

In Figure 3, the FR obtained from CxA is compared to one obtained from the continuation software Manlab [75, 72], which applies harmonic balancing (HBM) on the EOM, here for 10 harmonics. Both FRs coincide almost perfectly, with a slight discrepancy in the unstable fold of the FR, attributed to the inclusion of more harmonics in Manlab. This fully validates the analytical expression for the FR obtained here. Moreover, the excellent coincidence between the (one harmonic) analytical method derived from the CxA scheme and the numerical HBM (ten harmonics) comes from the fact that there is almost no harmonic distortion in the unknowns $(q(t), V(t))$ of the problem, such that the one harmonic assumption is almost perfect. The isola is by definition not computed automatically with Manlab (a dedicated condition would have been necessary to initiate the computation on the isola) and is was not found.

How the SIM, the FR and the bifurcations relate to the characteristic responses of a full numerical simulation of Eqs. (10) is investigated next.

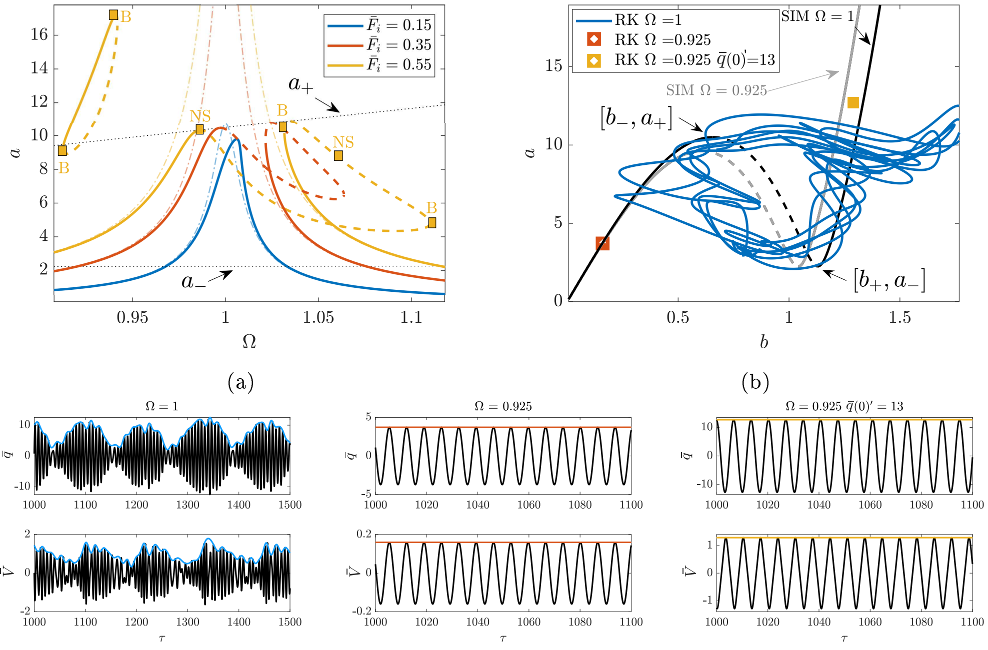

(a) (b)

(c) (d) (e)

Figure 2: Comparing FR and SIM to numerical simulations. (a) is the FR for $\bar{F}_i = [0.15, 0.35, 0.55]$, $r_i = k_i = \zeta_e = 0.2$ and $\zeta_i = 0.0073$ where the thick full lines are stable solutions, thick dashed lines are unstable solutions, thin line-dash lines are the open-circuit, and the thin dotted lines are the minimum and maximum of the SIM. (b) is the SIM for $\Omega = [0.925, 1]$ with envelopes of time evolutions of the full dynamical equations. (c-e) are time evolutions of the full dynamical equations which are also plotted on as a phase-space on (b).

3.2. *Characteristic responses*

The frequency responses in Figure 2a show that for increased force magnitude, the vibration amplitude of the host system folds around the saturation line of a_+, the maximum of the SIM. Once the FR folds over the saturation line, there is a NS bifurcation, which implies a quasi-periodic motion for the complete equations of motion. It can also be observed that for high forcing, here $\bar{F}_i = 0.55$, an isola appears in the frequency response, to the leftof the open-circuit resonance.

The full equation of motion, Eq.(8), for $\bar{F}_i = 0.55$ are simulated with a Runge Kutta (RK) scheme in Matlab (ODE45) for $\Omega = 1$, $\Omega = 0.925$ and $\Omega = 0.925$ and $\bar{x}(0)' = 13$, with the results shown in Figures 2c to 2e. The envelopes of the simulations, numerically computed from vibration signals using a Hilbert

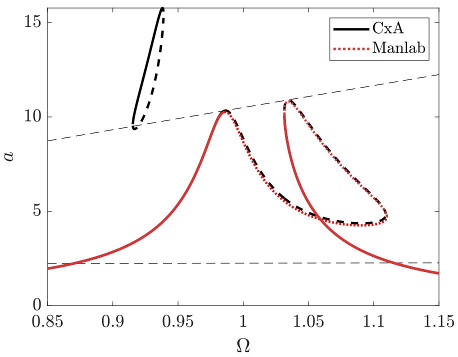

Figure 3: Comparison of the presented CxA technique and an established harmonic balancing Manlab which uses a continuation algorithm to solve. Manlab uses 10 harmonics.

transform, are plotted on a $a - b$ phase space, together with the SIMs on Figure 2b. The time simulation for $\Omega = 1$, Figure 2c, shows a quasi-periodic exchange between the modal displacement and voltage. This behavior is predicted by the NS bifurcation in the FR. In the context of mechanical NESs, this quasi-periodic exchange is called strongly modulated response (SMR). In the phase space, Figure 2b, the envelopes of the full dynamics follow, on average, the SIM. The envelope climb the left branch, then near the local maximum of the SIM, jumps the right branch. On the right branch, the dynamics descend the SIM, and jump back the left branch near the local minimum. For mechanical NES, this quasi-periodic motion and stability of the SIM are determined from a two-time scales scheme [38, 76, 77], which holds if the coupling ϵ is small. The stability for the SIM for piezoelectrical NES system is discussed in Appendix B. The SIM has a stable left branch, an unstable middle branch and a stable right branch. However, the two-time scales and the attraction of the full dynamics to the SIM (and thus the existence of quasi-periodic motions) depends on $\epsilon = r_i k_i$ being small. For the simulations, this holds as $\epsilon = 0.04$ and thus the SIM is indicative of the full EOM.

For $\Omega = 0.925$, the FR for $\bar{F}_i = 0.55$ has an isola, and for some frequency interval, there are two stable solutions. The time simulations on Figure 2d and 2e show that the initial conditions determine which part of the response is reached. For $\bar{q}_i(0) = 0$, the vibrations of the displacement and voltage are low. On the phase space, Figure 2b, the dynamics are on the left branch of the SIM. On the other hand, for $\bar{q}_i(0) = 13$, the response is on the isola, and both the modal and voltage vibration amplitude are high. The high response of the host system on the isola is thus not desired.

3.3. Numerical simulation over frequency band

The full EOM are now simulated with a stepped sine for $\bar{F}_i = 0.35$ and $\bar{F}_i = 0.75$, both for zero initial conditions, and are compared to the FR obtained from CxA on Figure 4. The envelopes are extracted from the RK simulation. When there is SMR, the maximum and minimum of the envelope are computed as well.

For $\bar{F}_i = 0.35$, Figure 4a, the numerical RK simulation and FR coincide well. After the NS-bifurcation, the simulations show SMR. During the SMR, the minimum and maximum amplitude correspond well with the lines of minimum and maximum SIM values, computed with Eq. (22). The FR does not estimate the RMS value of the simulation well. If the force is increased to $\bar{F}_i = 0.75$, Figure 4b, an isola appears and almost touches the main FR curve. The RK response jumps to the isola for some frequencies, even though no initial condition was applied in the simulation. This is to be expected, as it was also shown in [32] for mechanical NESs, if the isola (almost) touches the main branch in the FR obtained from CxA, the amplitude obtained RK simulation will end up on isola, even without initial conditions on $\bar{q}_i$. Jumping to the isola is to be avoided due to the high amplitude vibrations, and the NES shunt should be designed to avoid this.

Designing an NES shunt depends thus on the desired saturation amplitude, being a_+, but this will only hold as long as the isola doesn't grow too large and attaches or touches the main branch. The existence of the isola limits the useful forcing range. The isola is studied in more detail in the next section.

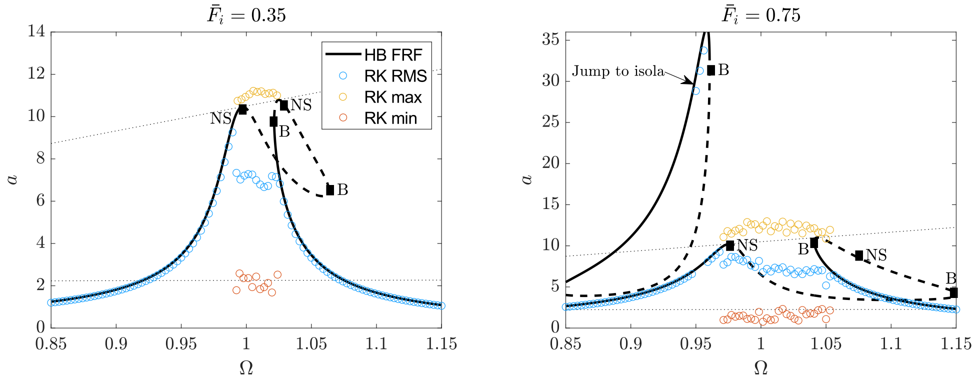

(a) (b)

Figure 4: Comparing FR with RK numerical simulations for $\bar{F}_i = [0.35, 0.75]$, $r_i = k_i = \zeta_e = 0.2$ and $\zeta_i = 0.0073$, where the thick full lines are stable solutions, thick dashed lines are unstable solutions, thin line-dash lines are the open-circuit, and the thin dotted lines are the minimum and maximum of the SIM. The blue is the RMS value times $\sqrt{2}$ of the RK simulation, and if there is quasi-periodic motion, orange and yellow circles minimum and maximum value of the envelope of the RK simulation.

3.4. Study of isola

The condition on Eq (19), called now $g(\Omega, \bar{F}_i)$ for convenience, for the onset of an isola is [78, 79]:

$$\frac{\partial g(\Omega, \bar{F}_i)}{\partial \Omega} = \frac{\partial g(\Omega, \bar{F}_i)}{\partial \bar{F}_i} = 0, \quad \frac{\partial^2 g(\Omega, \bar{F}_i)}{\partial \Omega^2} \neq 0, \quad \det(\partial^2 g(\Omega, \bar{F}_i)) > 0 \tag{23}$$

where $\det(\partial^2 g(\Omega, \bar{F}_i)) > 0$ is the determinant of the Hessian matrix. The Ω and $\bar{F}_i$ for where the condition is met reveal a single point that is the onset for an isola. For the system studied in Figure 2, this is for $\bar{F}_i = 0.539$ and $\Omega = 0.928$. For larger force levels, the isola grows as Figures of the FR, Figures 4b and 2a for $\bar{F}_i = 0.55$ and $\bar{F}_i = 0.75$ show. To better understand the conditions for isola and its relation to the saturation amplitude, the condition in Eq (23) is studied in Figure 5 for a range of ζ_e, r_i and k_i values. To have a large effective force range, the force $\bar{F}_i$ for which the isola appears, $\bar{F}_{\text{isola}}$, is preferably as high as possible. It is shown in Figure 5a in function of damping ζ_e. As the the damping ζ_e increases, $\bar{F}_{\text{isola}}$ increases until the condition (23) isn't met anymore. If the coupling factor k_i decreases or the frequency ratio r_i increases, $\bar{F}_{\text{isola}}$ is lower.

Equally important as $\bar{F}_{\text{isola}}$ is the amplitude of the host system on this isola, the corresponding saturation amplitude a_+ and the minimum of the SIM a_-. These are plotted for several r_i and k_i values on Figures 5b to 5d, along with the maximum amplitude of the FR for if $\bar{F}_i = 1.1 \cdot \bar{F}_{\text{isola}}$. The main effect of increasing the piezoelectric coupling k_i, (Figures 5b to 5c), is the decrease of saturation level a_+. The amplitude at the isola $a_{\bar{F}_{\text{isola}}}$ remains somewhat the same for a given ζ_e. Increasing r_i (Figures 5c to 5d) also leads to a decrease of a_+ while $a_{\bar{F}_{\text{isola}}}$ now also decreases. However, it can be seen that a_+ and a_- get closer, implying a smaller difference between the maximum and minimum amplitude during SMR, called the depth of SMR. To conclude, increasing the coupling factor k_i increases the force range the piezoelectric shunt is effective and decreases the saturation level a_+, but does not change much the amplitude at the isola. Increasing the frequency ratio r_i, however, decreases the effective force range but does lower both the saturation level and the amplitude at the isola. However, the increases of r_i will lead to a less 'deep' SMR. As such, an optimal NES shunt is a balance between force range, desired saturation, and depth of the SMR.

4. Experimental investigation

The analytical and numerical investigations of the previous sections will now be experimentally verified. First, the experimental setup is discussed, consisting of a cantilever beam as host system, and a measurement and exciter system. The beam's and piezoelectrical parameters are identified. Then, the nonlinear circuit and its limitations and realization are discussed in detail. Finally, the beam is

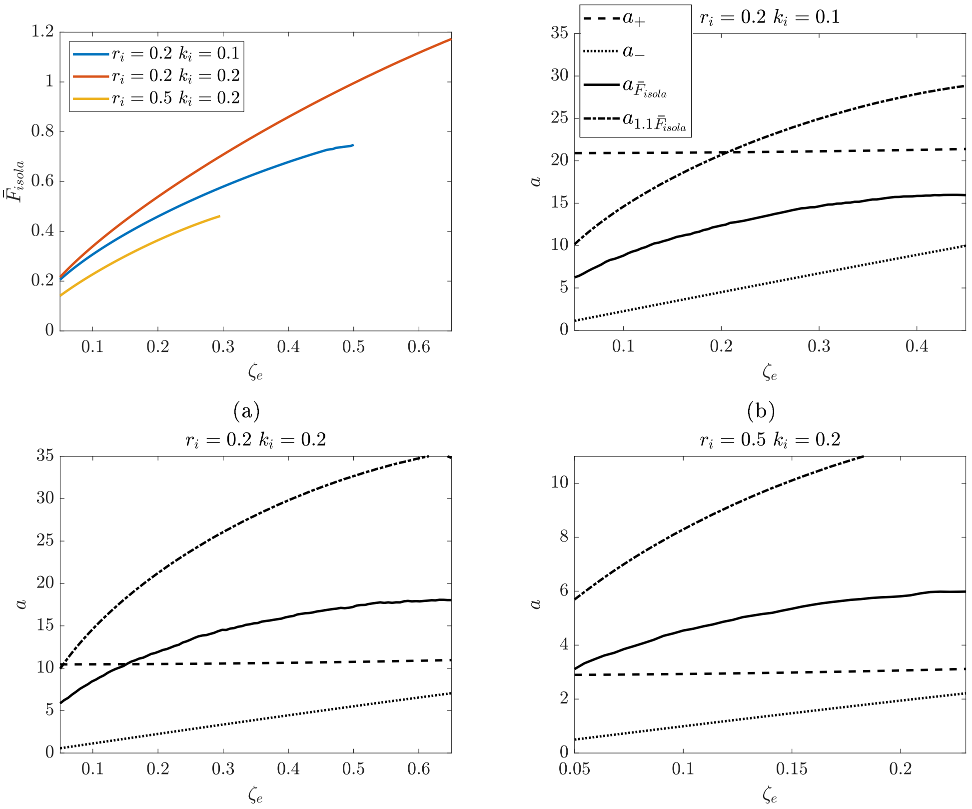

(a)

(b)

(c)

(d)

Figure 5: Effect of NES shunt parameters on the occurrence of the isola, (a) is the force $\bar{F}_i$ for which the isola appears, and (b), (c) and (d) show the modal amplitude a for this force level, $a_{\bar{F}_{\text{isola}}}$, the amplitude for a 10 % increase of the force, and the corresponding a_- and saturation level a_+.

excited experimentally by a stepped sine, and the experimental results with the NES shunt are compared to the analytical and numerical results.

4.1. Experimental setup and identification

A scheme of the setup is shown in Figure 6 while Figure 8 is the realization. A cantilever beam has two PIC 151 piezoelectric patches whose electrodes are connected to the nonlinear shunt. Figure 7 gives details of the beam's dimensions and shunt. The beam is 180 mm long, 30.5 mm wide and 1.1 mm thick. The PE patches are 70 mm long, 30.5 mm wide and 0.5 mm thick, and are bonded at the clamped end of the beam. A magnet is bonded with beeswax to the tip of the beam, and the magnetic field of a coil is used to apply a contactless force to the magnet. The current through the forcing coil has been shown to be proportional

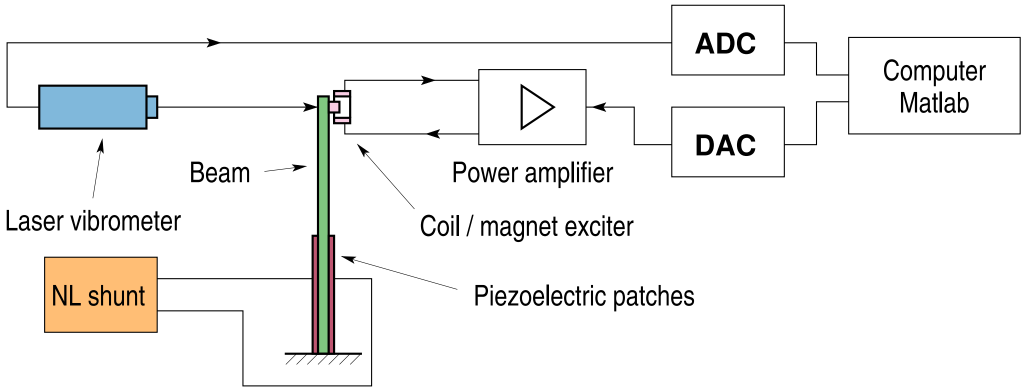

Figure 6: Scheme of experimental setup

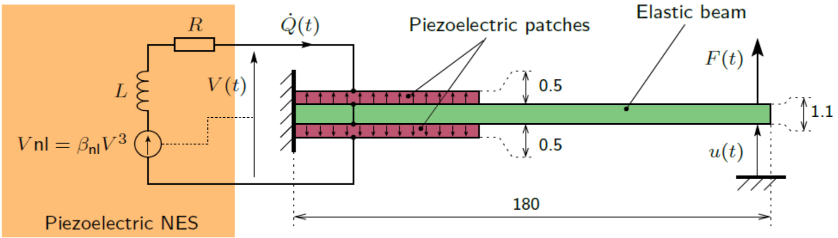

Figure 7: Scheme of the piezoelectric cantilever beam setup. Dimensions are in mm

to the applied force, $F(t) = \alpha I(t)$ [80]. A Brüel & Kjær 2719 power amplifier is used to generate a harmonic current with constant amplitude in the forcing coil. The velocity at the beam tip is measured with a Polytec OFC-505 laser vibrometer.

To experimentally obtain frequency responses, National Instruments cards (NI-9234 (ADC), NI-9263 (DAC)) are programmed by a Matlab script to apply a stepped sine to the current amplifier while concurrently measuring the velocity of the beam tip and the actual current in the forcing coil.

4.2. Host system identification

As a similar beam setup was used in [56], the same experimental identification was performed to re-obtain the modal parameters of the coupled beam/patch system. The values are reported in Table 1 and the experimental FRFs of the beam short- and open-circuit are given in Figure 9. Some values slightly differ from the reported values in [56], as the setup was reassembled and tested under slightly different clamping and environmental circumstances and a different forcing coil was used.

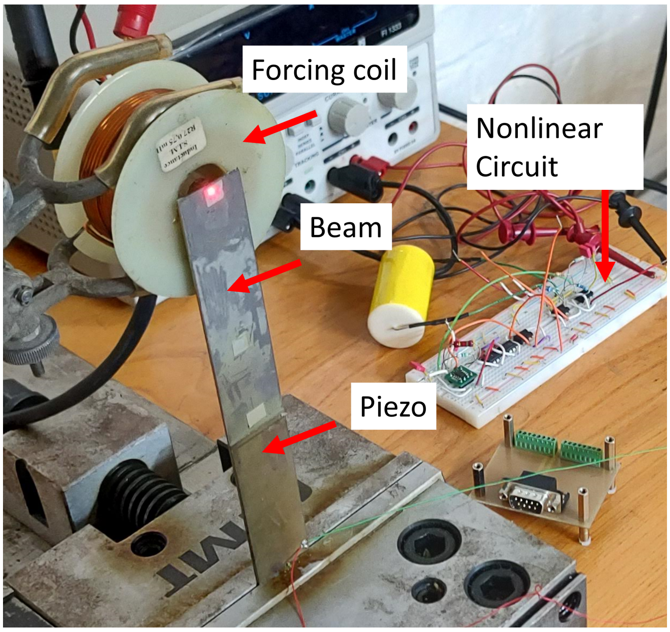

Figure 8: The setup, as realized in the lab.

Parameter	Identified value
$\omega_1/2\pi$ [Hz]	37.42
k_1 [$-$]	0.22
ζ_1 [%]	0.73
m_1 [g]	8.9
α [N/A]	0.056
C_p [nF]	32.45

Table 1: The identified values of the cantilever beam, the forcing coil and the capacitance of the piezo.

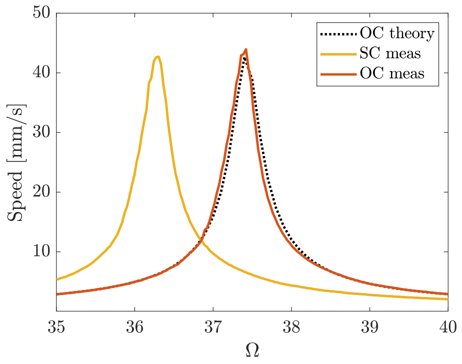

Figure 9: Experimental identified open- and short-circuit frequency response of the cantilever beam.

4.3. Nonlinear circuit

The circuits consist of an inductor, a resistor, and a nonlinear voltage source, with the scheme shown in Figure 10 and a picture of the implemented circuit in Figure 11. The NES parameters for the shunt will now be chosen. The goal is to show the expected NES behavior (saturation, SMR, and isola) experimentally rather than optimize towards some objective. In the discussion in section 3.4, it was found that a larger r_i will decrease the saturation level (k_i cannot be modified here, as the patches cannot move), but will also decrease the useful force range. To alleviate this, the damping ζ_e should be increased. However, a too-large damping might decrease the depth of the SMR. As such, it opted to design a shunt with $r_i = 0.5$ and $\zeta_e = 0.2$.

4.3.1. Inductor circuit

The inductor has to be quite large (1000s of Henry) to obtain the r_i. Therefore, it is opted for the Antoniou synthetic inductor as off-the-shelves passive inductors only have a value up to several 100 mH. It is composed of two operational amplifiers (OA) [81], as shown in Fig. 10. Considering an ideal model for the OAs, the equivalent inductance of the Antoniou circuit is:

$$L = \frac{R_1 R_2 R_4 C}{R_3}. \tag{24}$$

To obtain high inductance, large R_1, R_2, R_4 and C are required. However, the idealized inductance value does not hold if these values are too large and the Antoniou circuit might become unstable. Actually, the imperfections of each OA influence the bandwidth of the gyrator circuit and its stability. The main factor is the gain-bandwidth product of the OAs [82]. To realize $r_i = 0.5$ requires a 2200 H value with the components reported in Table 2 and two OPA 445 OAs (which

have a -+40 V range).
However, after identifying the inductance by attaching a 33 nF capacitance in series and doing a resonant test, it was found that the realized inductor has a value of 2080 H ($r_i = 0.52$). A resistance of 90 kΩ is added in series, that together with the equivalent resistance of the Antoniou circuit of about 15 kΩ, results in an equivalent resistance $R_e = 105\,\mathrm{k}\Omega$ and an electrical damping of $\zeta_e = 0.23$.

4.3.2. Nonlinear voltage source

To realize the nonlinear voltage source, a differential amplifier (DA) INA826 is used to measure the voltage at the terminals of the piezoelectric patches and two AD633 multipliers are used to create the cubic nonlinearity. The DA is necessary for three reasons. First, since the piezoelectric patches are not connected to the ground, it enables a floating measurement of $V(t)$. Secondly, it prevents discharging the piezoelectric capacitor due to the parasitic current that would be induced by the nonlinear circuit if it was directly connected. Finally, it enables the control of the input voltage of the multipliers, which are limited to 10 V. It opted to apply a force of $F = 1mN$, and to stay below the input voltage limit on the nonlinear voltage circuit due to high vibartions. RK simulation shows that this holds if the nonlinearity has a factor of $\beta_{\mathrm{nl}} = 4.4$. The output of the last multiplier is connected to a voltage follower, made with another OPA445 AO, in order to obtain a low output impedance. Note that a large R_5 resistor is inserted between the negative input of the DA and the ground to avoid DC polarization problems of the DA which would lead to saturation.

As reported in the datasheets, the INA826 [83] has a built-in gain of $1+\frac{49400}{R_g}$, controlled by an external resistor R_g. Since the output of an AD633 multiplier is equal to the product of its inputs divided by 10, combining an INA826 and two AD633 in series, the gain β_{nl} of the nonlinear voltage source is:

$$\beta_{\mathrm{nl}} = \frac{(1+\frac{49400}{R_g})^3}{10^2}. \tag{25}$$

In the experiments, $R_g = 7.5\ k\Omega$, resulting in $\beta_{\mathrm{nl}} = 4.4$, such that the saturation limits of the OPA445, AD633 and INA826 are respected for the forcing range that can be applied, while simultaneously also experimentally exhibiting the typical NES behavior as saturation, quasi-periodic oscillations and jumping to isola. The values of the electrical components are summarized in Table 2. From the mechanical and electrical parameters, the condition (23) is met for $\bar{F}_i = 0.38$ (or F=0.72 mN) at $\Omega = 0.937$.

4.4. Experimental results

4.4.1. Time measurements beam and characteristic responses

The measured beam tip velocity for a stepped sine forcing of $F = 0.92$ mN between 30 and 45 Hz in 450 s is shown in Figure 12a, and shows all the character-

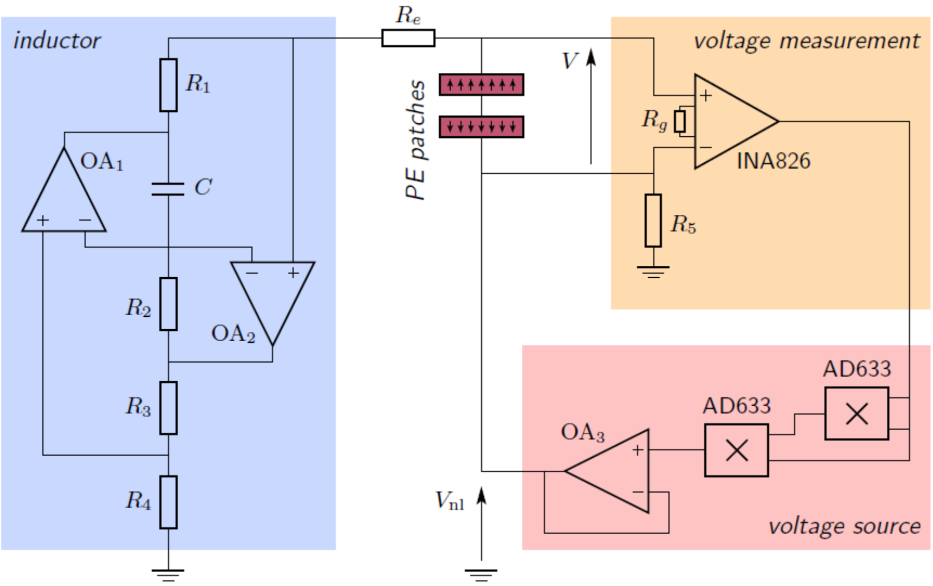

Figure 10: Electronic circuit that realizes the series connection of inductor, resistor and nonlinear voltage source.

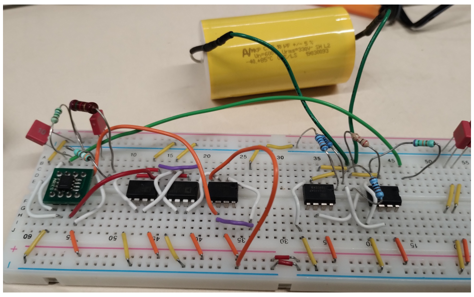

Figure 11: Picture of the nonlinear circuit on a breadboard.

Component	Value
R_1 [kΩ]	2
R_2 [kΩ]	1
R_3 [kΩ]	1
R_4 [kΩ]	110
C [μF]	10
R_5 [kΩ]	1000
R_g [kΩ]	7.5
Re [kΩ]	105
L [H]	2080
β_{nl} [1/V^2]	4.4
r_1 [-]	0.52
ζ_e [-]	0.21

Table 2: The values related to the nonlinear circuit.

istic behavior of the NES experimentally. The stepped sine is done in increments of 0.1 Hz, applied for 3 s each. The force level of $F = 0.92$ mN is above the force where the isola appears, and the measurement shows that the isola is reached between 93 and 180 s. Between 200 and 270 s, the amplitude saturates, and between 270 s and 360 s, the beam tip shows SMR, modulating the amplitude between a maximum and minimum value as dictated by the SIM. Figure 12b is a closer look at the piezoelectrical voltage and beam vibrations during SMR. This figure experimentally shows the exchange of vibration energy between the mechanical and electrical domains.

4.4.2. Frequency response and comparison with RK and CxA

Now, the FR is extracted from the measurements and it is compared to the FR obtained from CxA and the numerical RK simulation in Figure 13 for $F = 0.46$ mN and $F = 0.92$ mN. As the nonlinearity can introduce other harmonics in the response, at each frequency step, the amplitude of the first harmonic is extracted from the beam velocity signal with a synchronous demodulation procedure explained in detail in [56], while the minimum and maximum amplitude are obtained from the Hilbert transform on low-pass filtered measured signals. The analytical and numerical results are obtained for the identified parameters reported in Tables 1 and 2. The measurement and numerical simulation coincide well for both forcing levels, both regarding the existence of the isola and the saturation of the amplitude. Compared to the earlier numerical simulations in Figure 4b, the minimum and maximum SIM in dash lines in Figure 13 are not an as accurate predictor of minimum and maximum amplitude during SMR. This is

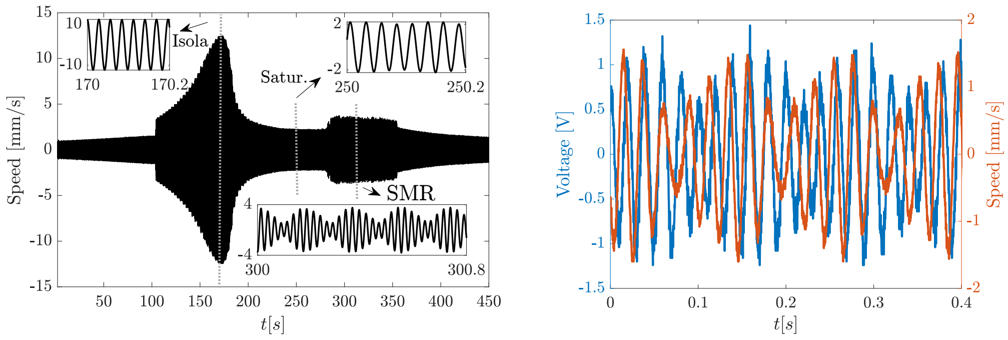

(a) (b)

Figure 12: (a) Experimental velocity as measured by the vibrometer for a force of $F = 0.92$ mN applied as a stepped sine between 30 to 45 Hz, in increments of 0.1 Hz applied for 3s each. (b) Measured quasi-periodic energy exchange between voltage and vibrations of the beam.

attributed to the relatively large $\varepsilon = r_i k_i$ of 0.14 here, while it was 0.04 in Figure 13. The larger ε is, the less the two-timing scheme and SIM (and thus Eq. (22)) is representative for the full dynamics [38, 76]. For all measurements shown in Figure 13, the beam saturates at the expected analytical and numerical level. Another set of measurements is presented in Figure 14. Figure 14a compares the measured open-circuit frequency response and the frequency response with the circuit for same force of $F = 0.77$ mN. This shows that the NES shunt 'cuts' the open-circuit FR, without creating two new peaks, which would be the case for linear shunts [41]. In Figure 14b, the experimental beam tip speed is plotted for several forces. The saturation of the speed remains at the same level, regardless of the forcing level. This is in contrast to the linear shunts, where the response would simply scale with the force. However, the speed is on the isola response for higher force amplitudes for frequencies just below the saturation region.

5. Conclusion

In this paper, a nonlinear energy sink shunt for piezoelectric vibration damping is investigated. Both analytical solutions, for vibration response prediction, and experimental validations, are provided. The shunt includes a standard resonant architecture (with inductor and resistor) in addition to a nonlinear voltage source proportional to the cube of the piezoelectric voltage, and realized in analog electronics with multipliers and operational amplifiers.

An analytical formulation was found for the frequency response by applying the complexification-averaging method. It was found that the observed behavior is similar to that of the mechanical NESs: 1) saturation of the host system's vibration amplitude around the original resonance frequency, regardless of force

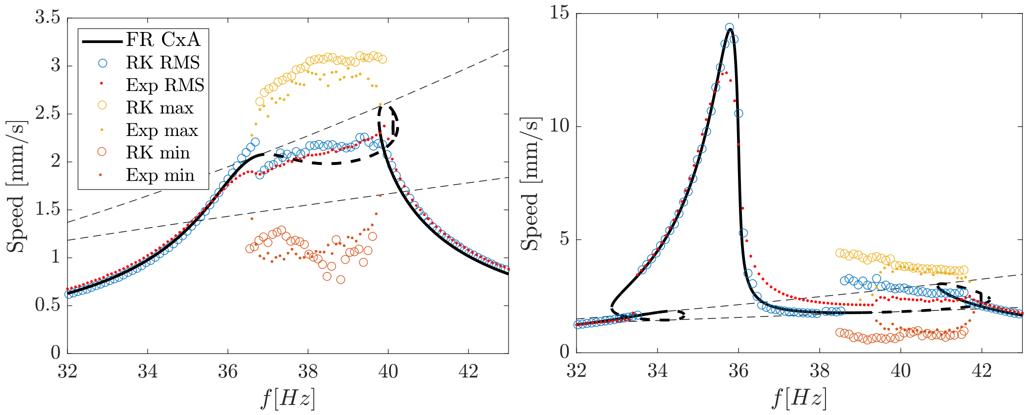

(a) (b)

Figure 13: Comparing experiments with FR and RK numerical simulations for $F = 0.46$ mN (a) and $F = 0.92$ mN (b). The thick full lines are stable solutions of the FR, thick dashed lines are unstable solutions, and the thin dotted lines are the minimum and maximum of the SIM. The blue is the RMS value times $\sqrt{2}$ of the RK simulation, and if there is quasi-periodic motion, orange and yellow circles are the minimum and maximum value of the envelope of the RK simulation. From the experiment, the red dots are the harmonic amplitude, and if there are quasi-periodic vibrations, the yellow dots and orange are the maximum and minimum amplitude.

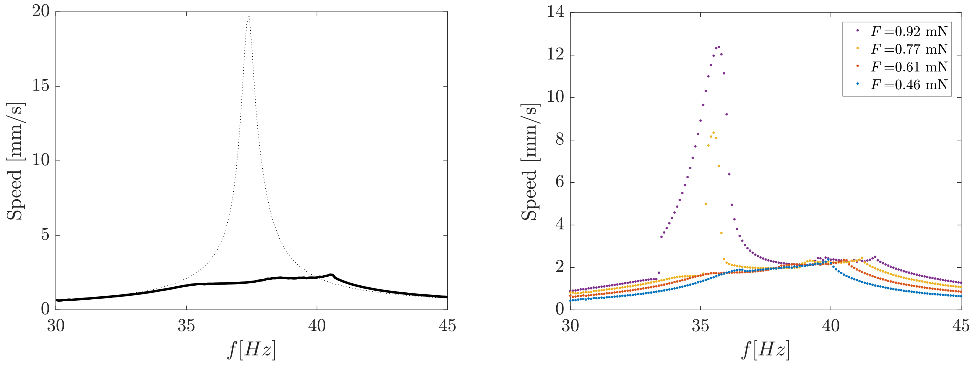

(a) (b)

Figure 14: (a) Comparison of the experimental open-circuit frequency response (dotted) and the frequency response with nonlinear circuit (full line) at the beam tip, for $F = 0.61$. (b) The frequency response with nonlinear circuit for $F = [0.46, 0.61, 0.77, 0.92]$ mN.

level, 2) strongly modulated response (SMR) near resonance, of which the motion is quasi-periodic between a minimum and maximum amplitude and is governed by a slow invariant manifold and 3) the existence of undesirable high-amplitude isolated responses for frequencies lower than host system's natural frequency. Although the saturation amplitude doesn't scale with the force level, the appearance of the isola does limit the effective force range. The appearance of the isola was then studied in relation to the NES shunt parameters. It was found that increasing the piezoelectrical coupling factor k_i increases the effective force range and decreases the host system's saturation amplitude. Increasing the ratio of mechanical and electrical eigenfrequencies, r_i, can further decrease this saturation amplitude but does decrease the effective force range. The other tuneable parameters, the electrical damping, increases the effective force range, but the difference between the minimum and maximum amplitude of the SMR decreased. Usually, the piezoelectrical coupling factor k_i is difficult to alter and as such, there is a balance between increasing the force range or a lower saturation amplitude of the host system.

These findings were then experimentally verified on a cantilever beam with two piezoelectric patches. The experimental circuit consisted of an Antoniou circuit to obtain the large inductance values, and the nonlinearity was realized by a differential amplifier and chaining two multipliers. The circuit parameters were chosen to showcase the amplitude saturation, the SMR, and the isolated responses for a given force range. An additional constraint was that the circuitry could only handle up to 10V input.

As a perspective, a more thorough optimized tuning can be investigated, which incorporates a desired force range, saturation amplitude in the forcing range, and the constraints on practical electric circuits. Other types of nonlinearities that typically occur in electronics can be investigated beyond polynomial voltage sources, as the cubic nonlinearity proposed here is inspired as an equivalence to mechanical NESs. Finally, other load cases, such as impulsive, can be studied to check the occurrence of resonance capture cascade.

Acknowledgements

Kevin Dekemele is funded by a post-doc fellowship of the Special Research Fund (BOF) from the Flemish Government awarded by Ghent University (BOF22/PDO/022).

References

[1] J. P. Den Hartog, Mechanical vibrations, Courier Corporation, 1985.

[2] R. Rana, T. Soong, Parametric study and simplified design of tuned mass dampers, Engineering structures 20 (3) (1998) 193–204.

[3] C.-L. Lee, Y.-T. Chen, L.-L. Chung, Y.-P. Wang, Optimal design theories and applications of tuned mass dampers, Engineering structures 28 (1) (2006) 43–53.

[4] M. Vakilinejad, A. Grolet, O. Thomas, A comparison of robustness and performance of linear and nonlinear lanchester dampers, Nonlinear dynamics 100 (2020) 269–287. `doi:10.1007/s11071-020-05512-x`.

[5] A. Roffel, S. Narasimhan, T. Haskett, Performance of pendulum tuned mass dampers in reducing the responses of flexible structures, Journal of Structural Engineering 139 (12) (2013) 04013019.

[6] V. Mahé, A. Renault, A. Grolet, H. Mahé, O. Thomas, On the dynamic stability and efficiency of centrifugal pendulum vibration absorbers with rotating pendulums, Journal of Sound and Vibration 536 (2022) 117157.

[7] J. Høgsberg, B. Lossouarn, J. F. Deü, Tuning of vibration absorbers by an effective modal coupling factor, International Journal of Mechanical Sciences 268 (2024) 109009.

[8] A. F. Vakakis, Inducing passive nonlinear energy sinks in vibrating systems, J. Vib. Acoust. 123 (3) (2001) 324–332.

[9] A. F. Vakakis, O. V. Gendelman, L. A. Bergman, D. M. McFarland, G. Kerschen, Y. S. Lee, Nonlinear targeted energy transfer in mechanical and structural systems, Vol. 156, Springer Science & Business Media, 2008.

[10] E. Gourdon, N. A. Alexander, C. A. Taylor, C.-H. Lamarque, S. Pernot, Nonlinear energy pumping under transient forcing with strongly nonlinear coupling: Theoretical and experimental results, Journal of sound and vibration 300 (3-5) (2007) 522–551.

[11] A. Ture Savadkoohi, B. Vaurigaud, C.-H. Lamarque, S. Pernot, Targeted energy transfer with parallel nonlinear energy sinks, part ii: theory and experiments, Nonlinear dynamics 67 (2012) 37–46.

[12] K. Dekemele, R. De Keyser, M. Loccufier, Performance measures for targeted energy transfer and resonance capture cascading in nonlinear energy sinks, Nonlinear Dynamics 93 (2) (2018) 259–284.

[13] K. Dekemele, P. Van Torre, M. Loccufier, Design, construction and experimental performance of a nonlinear energy sink in mitigating multi-modal vibrations, Journal of Sound and Vibration 473 (2020) 115243.

[14] G. Habib, F. Romeo, Tracking modal interactions in nonlinear energy sink dynamics via high-dimensional invariant manifold, Nonlinear Dynamics 103 (4) (2021) 3187–3208.

[15] K. Dekemele, G. Habib, Inverted resonance capture cascade: modal interactions of a nonlinear energy sink with softening stiffness, Nonlinear Dynamics (2023) 1–23.

[16] A. Malher, C. Touzé, O. Doaré, G. Habib, G. Kerschen, Flutter control of a two-degrees-of-freedom airfoil using a nonlinear tuned vibration absorber, Journal of Computational and Nonlinear Dynamics 12 (5) (2017) 051016.

[17] B. Bergeot, S. Bellizzi, S. Berger, Dynamic behavior analysis of a mechanical system with two unstable modes coupled to a single nonlinear energy sink, Communications in Nonlinear Science and Numerical Simulation 95 (2021) 105623.

[18] B. Bergeot, Effect of stochastic forcing on the dynamic behavior of a self-sustained oscillator coupled to a non-linear energy sink, International Journal of Non-Linear Mechanics 150 (2023) 104351.

[19] E. Gourc, S. Seguy, G. Michon, A. Berlioz, B. Mann, Quenching chatter instability in turning process with a vibro-impact nonlinear energy sink, Journal of Sound and Vibration 355 (2015) 392–406.

[20] G. Habib, T. Detroux, R. Viguié, G. Kerschen, Nonlinear generalization of den hartog' s equal-peak method, Mechanical Systems and Signal Processing 52 (2015) 17–28.

[21] G. Habib, G. Kerschen, A principle of similarity for nonlinear vibration absorbers, Physica D: Nonlinear Phenomena 332 (2016) 1–8.

[22] G. Raze, G. Kerschen, Multimodal vibration damping of nonlinear structures using multiple

nonlinear absorbers, International Journal of Non-Linear Mechanics 119 (2020) 103308.

[23] G. Habib, F. Romeo, The tuned bistable nonlinear energy sink, Nonlinear Dynamics 89 (1) (2017) 179–196.

[24] K. Dekemele, P. Van Torre, M. Loccufier, Performance and tuning of a chaotic bi-stable nes to mitigate transient vibrations, Nonlinear Dynamics 98 (2019) 1831–1851.

[25] H. Yao, Y. Cao, S. Zhang, B. Wen, A novel energy sink with piecewise linear stiffness, Nonlinear Dynamics 94 (2018) 2265–2275.

[26] C. da Silveira Zanin, A. T. Savadkoohi, S. Baguet, R. Dufour, G. Hurel, Nonlinear vibratory energy exchanges in a meta-cell, International Journal of Non-Linear Mechanics 146 (2022) 104148.

[27] S. Zhang, J. Zhou, H. Ding, K. Wang, Dual-power nonlinear energy sink for targeted energy transfer in ultra-wide range of impulsive energy, International Journal of Non-Linear Mechanics (2023) 104623.

[28] T. Roncen, G. Michon, V. Manet, Design and experimental analysis of a pneumatic nonlinear energy sink, Mechanical Systems and Signal Processing 190 (2023) 110088.

[29] J. E. Chen, M. Sun, W. H. Hu, J. H. Zhang, Z. C. Wei, Performance of non-smooth nonlinear energy sink with descending stiffness, Nonlinear Dynamics 100 (2020) 255–267.

[30] K. Dekemele, G. Habib, M. Loccufier, The periodically extended stiffness nonlinear energy sink, Mechanical Systems and Signal Processing 169 (2022) 108706.

[31] P.-O. Mattei, R. Côte, Optimization of a dynamic absorber with nonlinear stiffness and damping for the vibration control of a floating offshore wind turbine toy model, Journal of Theoretical, Computational and Applied Mechanics (2023).

[32] K. Dekemele, Tailored nonlinear stiffness and geometric damping: Applied to a bistable vibration absorber, International Journal of Non-Linear Mechanics 157 (2023) 104548.

[33] S. Charlemagne, C.-H. Lamarque, A. Ture Savadkoohi, Vibratory control of a linear system by addition of a chain of nonlinear oscillators, Acta Mechanica 228 (2017) 3111–3133.

[34] E. Boroson, S. Missoum, P.-O. Mattei, C. Vergez, Optimization under uncertainty of parallel nonlinear energy sinks, Journal of Sound and Vibration 394 (2017) 451–464.

[35] Y. Zhang, X. Kong, C. Yue, H. Xiong, Dynamic analysis of 1-dof and 2-dof nonlinear energy sink with geometrically nonlinear damping and combined stiffness, Nonlinear Dynamics 105 (1) (2021) 167–190.

[36] D.-D. Tan, Z.-Q. Lu, D.-H. Gu, H. Ding, L.-Q. Chen, A ring vibration isolator enhanced by a nonlinear energy sink, Journal of Sound and Vibration 508 (2021) 116201.

[37] Z.-Q. Lu, X.-Y. Chen, D.-D. Tan, F.-Y. Zhang, H. Ding, L.-Q. Chen, A hybrid linear dynamic absorber and nonlinear energy sink for broadband absorption of a circular ring, Nonlinear Dynamics 112 (2) (2024) 903–923.

[38] O. V. Gendelman, E. Gourdon, C.-H. Lamarque, Quasiperiodic energy pumping in coupled oscillators under periodic forcing, Journal of Sound and Vibration 294 (4-5) (2006) 651–662.

[39] E. Gourc, G. Michon, S. Seguy, A. Berlioz, Experimental investigation and design optimization of targeted energy transfer under periodic forcing, Journal of Vibration and Acoustics 136 (2) (2014) 021021.

[40] N. W. Hagood, A. Von Flotow, Damping of structural vibrations with piezoelectric materials and passive electrical networks, Journal of sound and vibration 146 (2) (1991) 243–268.

[41] O. Thomas, J. Ducarne, J.-F. Deü, Performance of piezoelectric shunts for vibration reduction, Smart Materials and Structures 21 (1) (2011) 015008.

[42] B. Lossouarn, M. Aucejo, J.-F. Deü, B. Multon, Design of inductors with high inductance values for resonant piezoelectric damping, Sensors and Actuators A: Physical 259 (2017) 68–76.

[43] K. Dekemele, P. Van Torre, M. Loccufier, High-voltage synthetic inductor for vibration damping in resonant piezoelectric shunt, Journal of Vibration and Control 27 (17-18) (2021) 2047–2057.

[44] M. Berardengo, O. Thomas, C. Giraud-Audine, S. Manzoni, Improved resistive shunt by means of negative capacitance: new circuit, performances and multi-mode control, Smart Materials and Structures 25 (7) (2016) 075033.

[45] L.-F. Lin, Z.-Q. Lu, L. Zhao, Y.-S. Zheng, H. Ding, L.-Q. Chen, Vibration isolation of mechatronic metamaterial beam with resonant piezoelectric shunting, International Journal of Mechanical Sciences 254 (2023) 108448.

[46] R. Darleux, B. Lossouarn, J.-F. Deü, Broadband vibration damping of non-periodic plates by piezoelectric coupling to their electrical analogues, Smart Materials and Structures, 29 (5) (2020) 054001.

[47] J. Gripp, D. Rade, Vibration and noise control using shunted piezoelectric transducers: A review, Mechanical Systems and Signal Processing 112 (2018) 359–383. `doi:10.1016/j.ymssp.2018.04.041`.

[48] P. Shivashankar, S. Gopalakrishnan, Review on the use of piezoelectric materials for active vibration, noise, and flow control, Smart Materials and Structures 29 (2020) 053001.

[49] P. Soltani, G. Kerschen, The nonlinear piezoelectric tuned vibration absorber, Smart Materials and Structures 24 (7) (2015) 075015. `doi:10.1088/0964-1726/24/7/075015`.

[50] B. Lossouarn, J.-F. Deü, G. Kerschen, A fully passive nonlinear piezoelectric vibration absorber, Philosophical Transactions of the Royal Society A: Mathematical, Physical and Engineering Sciences 376 (2127) (2018) 20170142.

[51] B. Lossouarn, G. Kerschen, J.-F. Deü, An analogue twin for piezoelectric vibration damping of multiple nonlinear resonances, Journal of Sound and Vibration 511 (2021) 116323.

[52] G. Raze, A. Jadoul, S. Guichaux, V. Broun, G. Kerschen, A digital nonlinear piezoelectric tuned vibration absorber, Smart Materials and Structures 29 (1) (2019) 015007.

[53] C. Richard, D. Guyomar, D. Audigier, G. Ching, Semi-passive damping using continuous switching of a piezoelectric device, in: Proc. of SPIE Smart Structures and Materials Conference: Passive Damping and Isolation, Vol. 3672, 1999, pp. 104–111.

[54] J. Ducarne, O. Thomas, J.-F. Deü, Structural vibration reduction by switch shunting of piezoelectric elements: modeling and optimization, Journal of Intelligent Material Systems and Structures 21 (8) (2010) 797–816.

[55] Z. A. Shami, C. Giraud-Audine, O. Thomas, A nonlinear piezoelectric shunt absorber with a 2:1 internal resonance: Theory, Mechanical Systems and Signal Processing 170 (2022) 108768. `doi:https://doi.org/10.1016/j.ymssp.2021.108768`.

[56] Z. A. Shami, C. Giraud-Audine, O. Thomas, A nonlinear piezoelectric shunt absorber with 2: 1 internal resonance: experimental proof of concept, Smart Materials and Structures 31 (3) (2022) 035006.

[57] Z. A. Shami, C. Giraud-Audine, O. Thomas, Saturation correction for a piezoelectric shunt absorber based on 2: 1 internal resonance using a cubic nonlinearity, Smart Materials and Structures (2023).

[58] Z. A. Shami, Y. Shen, C. Giraud-Audine, C. Touzé, O. Thomas, Nonlinear dynamics of coupled oscillators in 1:2 internal resonance: effects of the non-resonant quadratic terms and recovery of the saturation effect, Meccanica 57 (2022) 2701–2731. `doi:10.1007/s11012-022-01566-w`.

[59] V. Guillot, A. Ture Savadkoohi, C.-H. Lamarque, Tuning inter-modal energy exchanges of a nonlinear electromechanical beam by a nonlinear circuit, Archive of Applied Mechanics 92 (8) (2022) 2317–2349.

[60] O. Alfahmi, A. Erturk, Programmable hardening and softening cubic inductive shunts for piezoelectric structures: Harmonic balance analysis and experiments, Journal of Sound and Vibration 571 (2024) 118029.

[61] Z. A. Shami, C. Giraud-Audine, O. Thomas, A nonlinear tunable piezoelectric resonant shunt using a bilinear component: theory and experiment, Nonlinear Dynamics 111 (8) (2023) 7105–7136.

[62] B. Zhou, F. Thouverez, D. Lenoir, Essentially nonlinear piezoelectric shunt circuits applied to mistuned bladed disks, Journal of Sound and Vibration 333 (9) (2014) 2520–2542.

[63] T. M. Silva, M. A. Clementino, C. De Marqui Jr, A. Erturk, An experimentally validated piezoelectric nonlinear energy sink for wideband vibration attenuation, Journal of Sound and Vibration 437 (2018) 68–78.

[64] J. Mosquera-Sánchez, C. De Marqui Jr, Broadband and multimode attenuation in duffing- and nes-type piezoelectric metastructures, International Journal of Mechanical Sciences (2024) 109084.

[65] G. Zhao, G. Raze, A. Paknejad, A. Deraemaeker, G. Kerschen, C. Collette, Active nonlinear energy sink using force feedback under transient regime, Nonlinear Dynamics 102 (2020) 1319–1336.

[66] D. Bitar, E. Gourdon, C.-H. Lamarque, M. Collet, Shunt loudspeaker using nonlinear energy sink, Journal of Sound and Vibration 456 (2019) 254–271.

[67] O. Thomas, J.-F. Deü, J. Ducarne, Vibration of an elastic structure with shunted piezoelectric patches: efficient finite-element formulation and electromechanical coupling coefficients, International Journal of Numerical Methods in Engineering 80 (2) (2009) 235–268. `doi:10.1002/nme.2632`.

[68] ANSI/IEEE Std 176-1987, IEEE Standard on Piezoelectricity, The Institute of Electrical and Electronics Engineers, Inc., 1988.

[69] L. Manevitch, The description of localized normal modes in a chain of nonlinear coupled oscillators using complex variables, Nonlinear Dynamics 25 (2001) 95–109.

[70] O. Gendelman, Targeted energy transfer in systems with external and self-excitation, Proceedings of the Institution of Mechanical Engineers, Part C: Journal of Mechanical Engineering Science 225 (9) (2011) 2007–2043.

[71] D. Bitar, A. Ture Savadkoohi, C.-H. Lamarque, E. Gourdon, M. Collet, Extended complexification method to study nonlinear passive control, Nonlinear Dynamics 99 (2020) 1433–1450.

[72] L. Guillot, A. Lazarus, O. Thomas, C. Vergez, B. Cochelin, A purely frequency based floquet-hill formulation for the efficient stability computation of periodic solutions of ordinary differential systems, Journal of Computational Physics 416 (2020) 109477. `doi:10.1016/j.jcp.2020.109477`.

[73] Z. Wu, S. Seguy, M. Paredes, Qualitative analysis of the response regimes and triggering mechanism of bistable nes, Nonlinear Dynamics 109 (2) (2022) 323–352.

[74] L. Huang, X.-D. Yang, Dynamics of a novel 2-dof coupled oscillators with geometry nonlinearity, Nonlinear Dynamics 111 (20) (2023) 18753–18777.

[75] L. Guillot, B. Cochelin, C. Vergez, A taylor series-based continuation method for solutions of dynamical systems, Nonlinear Dynamics 98 (4) (2019) 2827–2845.

[76] O. Gendelman, Y. Starosvetsky, M. Feldman, Attractors of harmonically forced linear oscillator with attached nonlinear energy sink i: description of response regimes, Nonlinear Dynamics 51 (2008) 31–46.

[77] B. Vaurigaud, A. Ture Savadkoohi, C.-H. Lamarque, Targeted energy transfer with parallel nonlinear energy sinks. part i: Design theory and numerical results, Nonlinear dynamics 66 (2011) 763–780.

[78] G. Habib, G. I. Cirillo, G. Kerschen, Isolated resonances and nonlinear damping, Nonlinear Dynamics 93 (2018) 979–994.

[79] H. Guo, T. Yang, Y. Chen, L.-Q. Chen, Singularity analysis on vibration reduction of a nonlinear energy sink system, Mechanical Systems and Signal Processing 173 (2022) 109074.

[80] O. Thomas, C. Touzé, A. Chaigne, Asymmetric non-linear forced vibrations of free-edge circular plates, part 2: experiments, Journal of Sound and Vibration 265 (5) (2003) 1075–1101. `doi:10.1016/S0022-460X(02)01564-X`.

[81] L. von Wangenheim, Modification of the classical GIC structure and its application to

RC-oscillators, Electronic Letters 32 (1) (1996) 6–8.

[82] A. Antoniou, K. S. Naidu, Modeling of a gyrator circuit, IEEE Transactions on Circuit Theory CT-20 (5) (1973) 533–540.

[83] T. Instruments, INA826 Precision, 200-µA Supply Current, 3-V to 36-V Supply Instrumentation Amplifier With Rail-to-Rail Output, `https://www.ti.com/lit/ds/symlink/ina826.pdf`, [Online; accessed 10-January-2024] (2020).

Appendix A. Stability under harmonic load

The stability of the harmonic balanced solution in Eqs. (15) is computed from the eigenvalues of the Jacobian:

$$J = \begin{bmatrix} a_{11} & 0 & a_{13} & 0 \\ 0 & a_{22} & 0 & a_{24} \\ a_{31} & 0 & a_{33} & a_{34} \\ 0 & a_{42} & a_{43} & a_{44} \end{bmatrix} /2j\Omega \tag{A.1}$$

where

$$\begin{aligned} a_{11} &= -a_{22}^* = -(1 - k_i^2 - \Omega^2) - j2\zeta_i\Omega \\ a_{13} &= -a_{24}^* = -\frac{k_i}{r_i} \\ a_{31} &= -a_{42}^* = 2j\zeta_e r_i^2\Omega k_i - r_i k_i((1 - k_i^2) + 2j\Omega\zeta_i) \\ a_{33} &= -a_{44}^* = -(r_i^2 - \Omega^2) - 2j\zeta_e r_i\Omega - \frac{6}{4}BB^* - k_i^2 \\ a_{34} &= -a_{43}^* = -\frac{3}{4}B^2 \end{aligned} \tag{A.2}$$

Appendix B. Stability of SIM between *a* and *b*

The SIM relating a and b is vital in explaining the quasi-periodic behavior. The quasi-periodic behavior and stability of the SIM is explained with a two-time scale approach, as shown for mechanical NESs [32, 26, 77]. Two time scales are defined, $\tau_0 = \tau$ and $\tau_1 = \varepsilon\tau$, where $\varepsilon = k_i r_i \ll 1$. The terms in the first equation of Eqs. (15) are of $\mathcal{O}(\varepsilon)$ except for the first term, while the terms in the second equation are all of the same order. This leads to the following equations in $\mathcal{O}(\varepsilon^0)$:

$$\begin{aligned} &2j\frac{\partial A}{\partial \tau_0}\Omega = 0 \\ &2j\frac{\partial B}{\partial \tau_0}\Omega = -(r_i^2 - \Omega^2)B - \Omega^2 A k_i r_i - \Omega^2 A k_i r_i - 2\zeta_e r_i(j\Omega B - j\Omega A k_i r_i) + 3B^2B^* \end{aligned} \tag{B.1}$$

For values of $A = \frac{a}{2}e^{j\alpha}$ and $B = \frac{b}{2}e^{j\beta}$ that relate according to Eq. (17), the stability of the SIM is then computed by Jacobian of Eq. (B.1):

$$J = \begin{bmatrix} a_{11} & a_{12} \\ a_{21} & a_{22} \end{bmatrix} /2j\Omega \tag{B.2}$$

where

$$\begin{aligned} a_{11} &= -a_{22}^* = -(r_i^2 - \Omega^2) - 2j\zeta_e r_i \Omega - 6BB^* \\ a_{12} &= -a_{12}^* = -3B^2 \end{aligned} \tag{B.3}$$